Phase-Change Magnetic Memory: Rewritable Ferromagnetism by Laser Quenching of Chemical Disorder in $Fe_{60}Al_{40}$ Alloy

N. I. Polushkin,[1,2,*] V. Oliveira,[1,3] R. Vilar,[1] M. He,[4] M. V. Shugaev,[4] and L. V. Zhigilei[4,5]

[1]*Instituto Superior Técnico, Universidade de Lisboa, Av. Rovisco Pais, 1049-001 Lisboa, Portugal*
[2]*Institute for Physics of Microstructures of RAS, GSP 105 603950, Nizhny Novgorod, Russia*
[3]*Instituto Superior de Engenharia de Lisboa, Av. Conselheiro Emídio Navarro No. 1, 1959-007 Lisboa, Portugal*
[4]*Department of Materials Science and Engineering, University of Virginia, 395 McCormick Road, Charlottesville, Virginia 22904-4745, USA*
[5]*Department of Modern Functional Materials, ITMO University, 49 Kronverksky pr., St. Petersburg 197101, Russia*

(Received 16 October 2017; revised manuscript received 30 May 2018; published 17 August 2018)

High-intensity laser irradiation can effectively couple to practically all kinds of materials, causing modification of their physical properties due to laser-induced phase transformations. This gives rise to a broad field of laser micro- and nanofabrication with its various technological applications. We demonstrate that, in a 40-nm-thick film of $Fe_{60}Al_{40}$ alloy, a short laser pulse is capable of (re)writing the ferromagnetism observed at room temperature (RT). The energy of the pulse generating a ferromagnetic region has to be sufficiently high to induce melting of the $Fe_{60}Al_{40}$ layer, while the ferromagnetic state can be erased by various kinds of lower-intensity thermal treatment. This cycling of RT ferromagnetism can be explained in terms of the chemical order (B2)-disorder (A2) phase transition in the $Fe_{60}Al_{40}$ crystal lattice, which is affected by laser-induced melting and rapid resolidification. Our finding has implications for the development of a magnetic memory technology that would use the reversibility of the modulus of the magnetization vector instead of its direction. This promises to circumvent the problem of the superparamagnetic limit for magnetic data storage density.

DOI: 10.1103/PhysRevApplied.10.024023

I. INTRODUCTION

Interaction of strong laser radiation with solids and their surfaces is a long-standing research topic [1] that has given rise to intense studies of ultrafast phase transformations in the context of microfabrication [2,3]. In combination with a small object (e.g., a nanoparticle [4,5] or a tip of a scanning probe microscope [6,7]) placed near a solid surface subject to patterning, laser light can act as a source of the surface modifications produced through the optical near-field enhancement at the nanoscale (<100 nm) [8]. Various studies that address the direct laser-assisted patterning of small features contribute to the field of thermal nanolithography [9–11]. A particular kind of phase change that holds promise for laser nanostructuring of solid surfaces is crystallization or vitrification (or chemical ordering or disordering) of phase-change alloys [12–14]. If a phase transformation of this kind is accompanied by a reversible change of physical properties of the system, e.g., optical reflectivity or electrical resistivity, it can serve as a basis for manufacturing of next-generation memory devices that might have a relatively easy scaling path to reach densities exceeding those offered by current and future recording technologies. For example, information bits in conventional magnetic recording are limited in their sizes by thermal upsets of the magnetizations that occur when the bit sizes are below the superparamagnetic threshold [15]. An alternative approach to the magnetic storage technologies is to cycle (generate and delete) regions whose magnetic properties are different from those of a surrounding matrix [16–19]. In such patterned media, the bits of binary information are "larger magnetization" and "smaller magnetization", to still be distinguishable from each other under spontaneous changes of magnetization directions [17,20] as having different levels of the stochastic magnetic signal [21]. Recently, it has been demonstrated [17] that crystalline $Fe_{40}Ni_{38}Mo_4B_{18}$ films can be vitrified and then again crystallized by laser irradiation. Although all obtained states, with different chemical order, are ferromagnetic in such alloys, the detected difference in magnetic response is sufficient (approximately 5%) to be distinguishable with a magnetic sensor placed close to the film surface. Another phase-change magnetic material was uncovered by Song *et al.* [18], who demonstrated a nearly twofold reversible change of the saturation magnetization in $Fe_7Ge_{15}Sb_{33}Te_{45}$ thin films induced by

*Email: nip@ipmras.ru

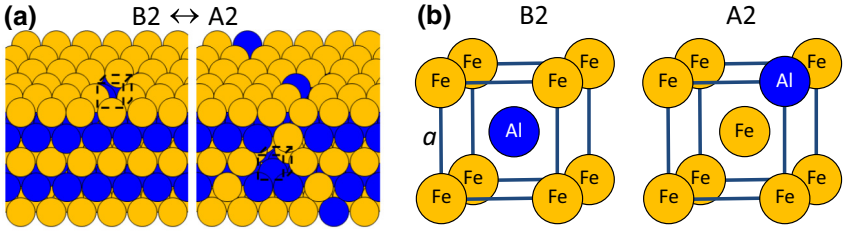

FIG. 1. $Fe_{60}Al_{40}$ structure. (a) Ordered B2 and disordered A2 structures in the bcc $Fe_{60}Al_{40}$ lattice. The B2–A2 transition can proceed through atomic jumps between Fe and Al-rich planes via the vacancy diffusion mechanism (vacancies are indicated by the dashed boxes). (b) The bcc unit cell in $Fe_{60}Al_{40}$. In the A2 phase, an Fe atom appearing in the cube center has Fe neighbors at a closer distance of $a\sqrt{3}/2$, where a is the lattice constant. This atomic configuration provides bigger overlap of electron d orbitals, which is responsible for the enhancement of ferromagnetism.

short-pulse laser irradiation. Even a much higher contrast in the magnetic properties, from ferrimagnetic to antiferromagnetic state, has been achieved and attributed to the order-disorder phase transition in the $FeMnP_{0.75}Si_{0.25}$ compound synthesized in the bulk form [19].

Here we consider thin films of binary alloys with chemical order-disorder transition, a class of materials which can be of interest in view of phase-change magnetic memory. We demonstrate that room-temperature (RT) ferromagnetism in a 40-nm-thick film of $Fe_{60}Al_{40}$ alloy is rewriteable and reveal the physical conditions required for writing and erasing ferromagnetic regions within the film. A short laser pulse with energy sufficient for transient melting of an $Fe_{60}Al_{40}$ film, which initially has nearly zero magnetic response at RT, is capable of producing the ferromagnetism within the laser spot [22]. This ferromagnetic state can be deleted by applying different types of lower-intensity (below melting) heat treatments, e.g., standard thermal annealing, high-density electric current, or a train of laser pulses, and then recovered by subsequent high-intensity laser irradiation. The material selected for probing thermally induced phase transformations, $Fe_{60}Al_{40}$, is well established [23–35] to exhibit the chemical reversible order-disorder (B2-A2) phase transition, which occurs via atomic jumps between adjacent Fe- and Al-rich planes through the vacancy diffusion mechanism [23–25]. It has been previously demonstrated experimentally [26–34] and supported by first-principles calculations [35–37] that the ordered B2 state [Fig. 1(a)] in $Fe_{60}Al_{40}$ alloy is non(ferro)magnetic [38]. Transformation of the chemically ordered B2 into disordered A2 state leads to an increase in the number of nearest Fe-Fe neighbors [Fig. 1(b)] and provides thus the enhancement of ferromagnetism [26–35] due to bigger overlapping of electron d orbitals between the Fe atoms occupying centers and vertexes of the bcc $Fe_{60}Al_{40}$ lattice [34,39]. It has also been argued [28] that the magnetic percolation between Fe atoms in the $Fe_{60}Al_{40}$ alloy leads to the emergence of long-range ferromagnetic order. This picture is consistent with vast evidence that the ferromagnetism in $Fe_{60}Al_{40}$ is highly influenced by structural defects, e.g., antiphase boundaries [26,33]. Previously, the disordering and, thus, the onset of ferromagnetism were achieved through various kinds of treatments, e.g., cold working [26,27], ball milling [28–30], and ion irradiation [31,32]. The produced ferromagnetism can be suppressed (through chemical ordering) with standard thermal annealing in a temperature range of 400–1000 K [29,31]. In our work, we show that the ferromagnetism in $Fe_{60}Al_{40}$ is also rewritable with short-pulse laser irradiation. This finding is promising for applications utilizing compact and inexpensive laser sources for magnetic recording technologies.

II. METHODS

A. Sample preparation and characterization

Polycrystalline films of $Fe_{60}Al_{40}$ composition and 40 nm thickness are prepared by magnetron sputtering from an $Fe_{60}Al_{40}$ target onto thermally oxidized Si(100) substrates [31]. In order to obtain the initial ideally nonmagnetic state (B2-ordered phase), the sputtered samples are thermally annealed at 1×10^{-5} mbar in a vacuum-annealing furnace in a temperature range of 700–800 K [31]. After annealing, the grain diameter increases up to approximately 15 nm, which is determined with the Scherrer equation from grazing-incidence x-ray diffraction (GIXRD) patterns. In laser irradiation of the postannealed samples, we use nanosecond and femtosecond pulses with incident fluence of up to 1 J/cm^2. In these experiments, the third harmonic ($\lambda = 355$ nm) of a nanosecond Q-switched Nd:YAG laser (EKSPLA) as well as the fundamental line ($\lambda = 1030$ nm) of an Amplitude Systèmes laser system with pulse duration of 500 fs are employed. Magnetic properties of the as-prepared, thermally annealed and laser-irradiated samples are probed with the longitudinal magnetooptic Kerr effect (MOKE). To observe the MOKE, the probing beam from a laser-diode module, operating at a wavelength of $\lambda = 670$ nm with a power of 5.5 mW, is focused on the film surface.

B. Simulation

The kinetics of laser-induced heating and cooling is studied with a conventional two-temperature model (TTM) [40] enhanced with computational treatment of melting and resolidification occurring under nonequilibrium conditions of superheating or undercooling, as well as the heat transfer from the film to the substrate. The TTM provides a continuum-level description of the laser excitation and subsequent relaxation of the conduction-band electrons. The equations of the TTM model are solved using the backward (implicit) Euler algorithm based on the block tridiagonal matrix inversion. The simulations are performed for a computational system consisting of a 40 nm $Fe_{60}Al_{40}$ film on a 2-μm-thick silicon substrate covered by a 150-nm-thick SiO_2 layer. A detailed description of the model is given in Refs. [41,42], and below we only outline the parameters relevant for the current setup.

The irradiation of the target by a 500-fs laser pulse is represented through a source term added to the TTM equation for the electron temperature. The source term accounts for the excitation of the conduction-band electrons by a laser pulse with a Gaussian temporal profile and reproduces the exponential attenuation of laser intensity with depth under the surface (Beer-Lambert law), with the optical absorption depth of 19 nm assumed to be the same as for pure Fe at the laser wavelength of 1030 nm [43]. Since the laser spot size used in the experimental setup is much larger than the heat-diffusion length during the time of melting and resolidification, approximately 1 μm, we assume the one-dimensional heat transfer along the direction normal to the sample surface.

Since the available temperature dependencies of electron heat capacity and electron-phonon coupling accounting for the contribution from the thermal excitation from the electron states below the Fermi level are mostly limited to pure metals [44], the dependences calculated for α-Fe [45] are used in the simulations performed for the $Fe_{60}Al_{40}$ alloy. Similarly to Ref. [41], the temperature dependence of the electron thermal conductivity is approximated by the Drude model relationship, $K_e(T_e, T_l) = v^2 C_e(T_e)\tau_e(T_e, T_l)/3$, where $C_e(T_e)$ is the electron heat capacity, v^2 is the mean-square velocity of the electrons contributing to the electron heat conductivity, approximated in this work as the Fermi velocity squared, ${v_F}^2$, and $\tau_e(T_e, T_l)$ is the total electron scattering time defined by the electron-electron scattering rate, $1/\tau_{e\text{-}e} = AT_e^2$, and the electron-phonon scattering rate, $1/\tau_{e\text{-ph}} = BT_l$, so that $1/\tau_e = AT_e^2 + BT_l$. The value of the coefficient A (8.9×10^5 $K^{-2}\,s^{-1}$) is estimated within the free-electron model. The coefficient B is described as a function of the lattice temperature, so that the experimental temperature dependences of the thermal conductivity of the $Fe_{60}Al_{40}$ alloy [46,47] under the conditions of electron-phonon equilibrium are reproduced in the simulations.

A single "melting" temperature of the $Fe_{60}Al_{40}$ alloy, $T_m = 1662$ K, approximated as an average of solidus and liquidus temperatures [48], is used to simplify the description of melting and resolidification processes in the model. The temperature dependence of the velocity of the liquid-crystal interface is described by the Wilson-Frenkel expression [49] with parameters taken for the Fe (100) interface from Ref. [50]. Since pure Fe has different melting temperature than the $Fe_{60}Al_{40}$ alloy, the diffusion activation energy and the heat of fusion are renormalized based on the T_m of the alloy to ensure the same velocity of the interface at the same values of relative undercooling T/T_m:

$$V_I = V_0 \exp(-\tilde{Q}T_m/T)\{1 - \exp[-\tilde{H}_f\,(T_m/T - 1)]\},$$

where V_0 is a prefactor equal to 2200 m/s, $\tilde{Q} = Q^{\mathrm{Fe}}/k_B T_m^{\mathrm{Fe}} = 1.23$ is the reduced diffusion activation energy, and $\tilde{H}_f = H_f^{\mathrm{Fe}}/k_B T_m^{\mathrm{Fe}} = 0.884$ is the reduced heat of fusion. To account for fast homogeneous melting of a strongly superheated solid, the regions of the target where the lattice temperature exceeds $1.3T_m$ are set to undergo instantaneous melting. If liquid is undercooled below $0.7T_m$, the onset of homogenous solidification is assumed, and the liquid transforms into a solid state. The lattice heat capacity of the alloy is assumed to be equal to $3R$ and is calculated based on the lattice parameter $a = 0.29$ nm of $Fe_{60}Al_{40}$ B2 structure, e.g., Ref. [28], which gives 3.4×10^6 J/m^3 K. The heat of fusion is estimated as a weighted average of values for Al and Fe based on the composition of the alloy, yielding 1.7×10^9 J/m^3.

The heat capacities of Si and SiO_2 (silica) are assumed to be equal to 1.66×10^6 and 1.63×10^6 J/m^3 K, respectively [51], while the thermal conductivities are fitted to the experimental temperature dependences provided in Ref. [51]. Since the value of interfacial thermal conductance depends not only on the materials in the contact but also on the method of the film deposition, it cannot be reliably evaluated without direct experimental measurements. Therefore, the thermal conductance of the $Fe_{60}Al_{40}/SiO_2$ interface is assumed to be 10^8 W/m^2 K, which is a typical value measured for metal-oxide interfaces in experiments [52]. The value of the thermal conductance of the SiO_2/Si interface is taken as 2.5×10^9 W/m^2 K [53].

III. RESULTS

Experimentally, we study $Fe_{60}Al_{40}$ films sputtered at RT onto thermally oxidized Si (100) substrates (SiO_2/Si) with sizes of 10×10 mm^2. As-prepared samples are thermally annealed at $T = 773$ K (TA treatment) for their successive treatment by laser irradiation. Figure 2(a) shows magnetization curves obtained by measuring the MOKE at RT in a TA $Fe_{60}Al_{40}$ film (a sample subjected to the TA treatment) [31] and after irradiation of this sample by a 5-ns pulse

delivered to the sample surface by a multimode laser beam [54] with incident fluence close to the ablation threshold (approximately 0.5 J/cm^2). The ablation induced by the nanosecond laser with the multimode beam is detected with an optical microscope as the appearance of multiple damaged locations within a spot with diameter of a few tens of micrometers on the film surface.

With our MOKE setup, we observe a nearly zero MOKE response (signal-to-noise ratio is about 1:1) from a TA $Fe_{60}Al_{40}$ film in applied magnetic field up to $\mu_0 H =$ 70 mT [inset in Fig. 2(a)]. We see, however, that this sample irradiated by laser exhibits a strong MOKE response, comparable to that from a film of pure α-Fe (approximately 0.1° in Kerr rotation), while the hysteresis loop measured is typical for structurally homogeneous ferromagnetic materials. We also see that the MOKE response after irradiation by the laser is close to that after irradiation by 25-keV Ne^+ ions [31]. The saturation magnetization of the sample irradiated by the ion beam is measured to be 0.98 T [31]. This strongly ferromagnetic state can be suppressed, in particular, by repeating the TA treatment [38]. In Fig. 2(b) we demonstrate cycling of the RT MOKE response, which reflects an extent of the chemical order, under successive application of the TA treatment and laser irradiation. In the experiments, we produce ferromagnetic regions in a TA $Fe_{60}Al_{40}$ sample, which are erased by repeating the TA procedure and then are recovered by laser. Alternatively, a high-density electric current passing through a μm-scale paramagnetic $Fe_{60}Al_{40}$ stripe [55] or a train of lower-intensity laser pulses [56] can be used for erasing ferromagnetic regions produced by single high-intensity laser pulses, as shown schematically in Fig. 2(c).

Analysis of the microstructure with GIXRD is used to confirm the relationship between the magnetic order and structural transformation in the $Fe_{60}Al_{40}$ system. Figure 2(d) shows GIXRD scans taken at a 1° grazing angle of the incident x-ray beam for a TA $Fe_{60}Al_{40}$ sample and after its subsequent nanosecond laser irradiation in the regime that provides the enhancement of ferromagnetism [Figs. 2(a) and 2(b)]. In order to collect GIXRD patterns of laser-irradiated samples, we scan the whole sample surface by the laser beam. In addition, we show a GIXRD

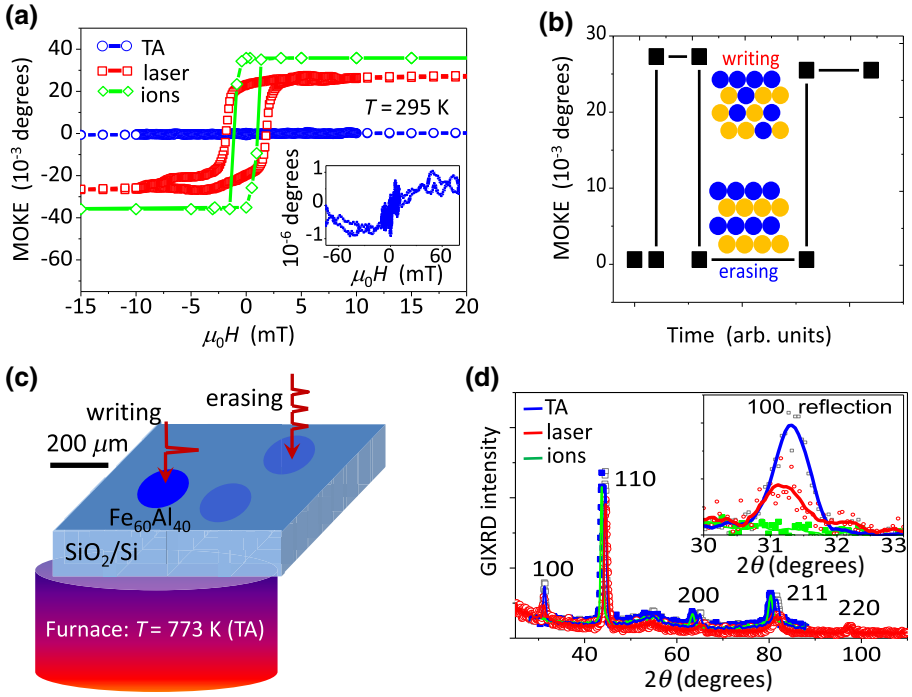

FIG. 2. Laser-induced ferromagnetism. (a) MOKE hysteresis loops taken at RT of a TA $Fe_{60}Al_{40}$ sample and after its irradiation by a 5-ns laser pulse with an incident fluence close to the ablation threshold, approximately 0.5 J/cm^2. For comparison, we show the MOKE response of the same sample irradiated by 25-keV Ne^+ ions [31]. The inset depicts the MOKE response of a TA $Fe_{60}Al_{40}$ film in applied fields of up to $\mu_0 H \sim 100$ mT. (b) Cycling of the MOKE response under successive application of the TA treatment and laser irradiation. (c) Schematic of laser writing of strongly ferromagnetic regions with a high-fluence laser pulse as well as of their suppression with thermal treatments of different kinds at moderate temperatures, e.g., thermal annealing in a furnace (TA treatment) or with a train of lower-intensity laser pulses [56]. (d) GIXRD scans of a TA $Fe_{60}Al_{40}$ sample and after its irradiation with a nanosecond laser pulse near the ablation threshold, as well as after its irradiation by 25-keV Ne^+ ions [31]. The inset shows laser- and ion-induced degradation of the superstructure in the ordered B2 phase. The x-ray data is collected after nanosecond laser irradiation that produces the transformation through the whole sample area by scanning over it in the multishot regime.

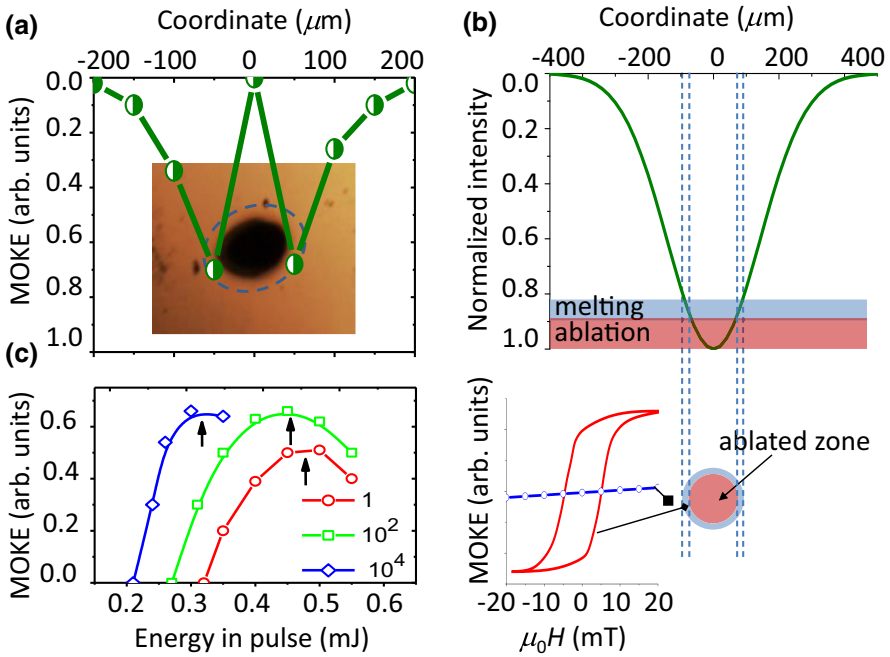

FIG. 3. Correlation of MOKE response with transient melting of $Fe_{60}Al_{40}$. (a) Distribution of the MOKE response over the spot on the sample surface irradiated by a 500-fs laser pulse with energy above the threshold for ablation. The inset depicts an optical image of the irradiated spot with ablated zone (dark spot) and surrounding ring-shaped ferromagnetic zone outlined by the dashed contour. (b) The Gaussian profile of the laser beam with indication of the ablation zone and the $Fe_{60}Al_{40}$ ring with the modified properties. A strong MOKE response and ferromagnetic hysteresis is detectable at RT inside the ring, while the signal is absent or at least weakly ferromagnetic [38] (slightly tilted line) at a film location close to the ring. (c) Dependence of the MOKE response on the pulse energy for a different number of 500-fs laser pulses: 1, 10^2, and 10^4. The arrows indicate the thresholds for ablation.

scan for a similar TA $Fe_{60}Al_{40}$ sample that was irradiated by Ne^+ ions for chemical disordering of the alloy and thus for achieving the ferromagnetism induced by the ion beam [31]. We see that strong laser irradiation induces a transformation that is similar to that occurring under ion irradiation, i.e., chemical disordering of the crystal structure [31]. Indeed, both kinds of treatment give reduction of the (100) reflection from the superstructure (shown in the inset in greater detail), which indicates the reversible [Fig. 2(b)] transformation of the nearly nonmagnetic, structurally ordered, B2 state into the ferromagnetic, structurally disordered, A2 phase.

Interestingly, we find that the ferromagnetism in a TA $Fe_{60}Al_{40}$ sample can be induced even with a femtosecond laser. Figure 3(a) shows the distribution of the MOKE response along a location on the surface of a TA $Fe_{60}Al_{40}$ film irradiated by a 500-fs pulse with an incident fluence above the ablation threshold, which is approximately 0.4 J/cm^2 for this pulse duration. In order to retrieve the distribution of the MOKE response, the light beam from the femtosecond laser system is focused onto the sample surface with a 30-cm focal-length lens. The magnetization in the irradiated zone is probed with a MOKE beam focused onto the spot with a diameter of approximately 30 μm. In order to explain the obtained MOKE distribution, Fig. 3(b) depicts the femtosecond-laser-beam profile approximated as $\exp(-2\rho^2/D^2)$, where ρ is the distance from the laser spot center and $D = 400$ μm is the laser spot diameter (full with at half maximum). The melted and ablated zones as well as the corresponding MOKE response are shown at the bottom of Fig. 3(b). We see that the MOKE response (and thus magnetization) is maximal at the periphery of the ablated region, while the measured hysteresis loop is close to that observed after irradiation by a nanosecond laser pulse [Fig. 2(a)]. The MOKE intensity quickly decays with increasing distance from its edge. Thus, the patterned ferromagnetic region is ring-shaped and adjacent to the ablated zone, suggesting that melting of the $Fe_{60}Al_{40}$ material is needed for the formation of ferromagnetic state upon resolidification and cooling down to RT. This conclusion correlates with the results of simulations of laser-induced phase transformations in metallic targets (e.g., Ref. [57]), which predict the melting fluence threshold to be several times lower than the threshold for spallation and ablation.

We also note that the pronounced MOKE response is also achievable with a single femtosecond pulse irradiation below the ablation threshold [Fig. 3(c)]. In the multishot regime, with a pulse repetition rate of 10^4 Hz and with the number of pulses increasing to 10^2 and 10^4, the

MOKE response further enhances. However, its increase is limited by ablation of the $Fe_{60}Al_{40}$ film. The ablation thresholds are established through optical microscopy measurements and are indicated by the arrows in Fig. 3(c). As the number of shots increases, the ablation threshold shifts toward the lower values of laser energy, suggesting that the ablation of the thin $Fe_{60}Al_{40}$ film exhibits the so-called incubation effect that has been reported, for instance in Ref. [58]. It is interesting to note that a train of 10^4 femtosecond laser pulses initiates ablation at a pulse energy that is still insufficient to induce a nonzero MOKE response with a single pulse and is, presumably, below the melting threshold with a single pulse. This difference between the results obtained in the single- and multishot regimes indicates the cumulative effect of multiple shots on the onset of melting and ablation.

IV. DISCUSSION

The experimental results described above suggest that short-pulse laser irradiation produces chemical disordering in the $Fe_{60}Al_{40}$ bcc crystal lattice above the critical temperature T_c for the order-disorder transition. According to the Fe-Al phase diagram [48] that shows the ordered B2 phase to be the equilibrium state of the $Fe_{60}Al_{40}$ alloy below $T_c = 1563$ K for the A2-B2 transformation, which is only 5% below the solidus temperature of the alloy [48] (a single "melting temperature," $T_m = 1662$ K, defined here as the average between the solidus and liquidus temperatures of 1642 and 1682 K, respectively, is used in this paper to simplify the discussion and modeling). The disordering is observed in the regions that are likely to undergo transient melting followed by resolidification, and the disordered state in these regions manifests itself by exhibiting ferromagnetism after cooling to room temperature. This observation, however, leads to the question of why the disordered state (and thus ferromagnetism) persists in the sample, while heat treatment at a much lower $T = 773$ K (TA treatment) readily produces chemical ordering (Fig. 2). The formation of chemically disordered structures by rapid solidification by itself is not surprising and has been considered theoretically [59] and observed experimentally [60–62] even for alloys with $T_c > T_m$, where a strong driving force for ordering exists at any level of undercooling. For $Fe_{60}Al_{40}$, where $T_c < T_m$, the chemical disorder can be readily trapped by the advancing solidification front, and the transformation to the ordered phase can be expected to occur through the diffusional atomic rearrangements in the solid state.

In order to revel the physical conditions leading to the generation and survival of the chemically disordered state in the irradiated film, we perform a series of continuum-level simulations of melting and resolidification of a 40-nm-thick $Fe_{60}Al_{40}$ film deposited on a SiO_2(150 nm)/Si substrate and irradiated with a 500-fs laser pulse. These simulations allow us to evaluate the cumulative atomic diffusion length in the $Fe_{60}Al_{40}$ alloy after its resolidification. The computational model is described in Sec. II, and the simulation conditions mimic the ones of experiments used for collection of data presented in Fig. 3.

The surface temperature (T_s) profiles shown in Figs. 4(a)–4(c) for three values of the absorbed laser fluence (F_{abs}) clearly demonstrate the strong effect of melting on the thermal history of the surface region of the film after the solidification and, therefore, on the extent of atomic rearrangements that can take place during the cooling of the solidified surface. The variation of the intensity of color in the colored areas under the temperature profiles provides a visual representation of the temperature dependence of the atomic mobility in the solid state. In the simulations where complete or partial melting takes place, Figs. 4(a) and 4(b), the reordering starts only after the resolidification and cooling down below T_c, if T_c is lower than the temperature reached at the end of resolidification [Fig. 4(b)]. It is notable that the conditions of partial melting [Fig. 4(b)] provide more time for the active high-temperature diffusion after the end of resolidification as compared to the complete melting [Fig. 4(a)], when the liquid is undercooled down to a lower temperature before the homogeneous crystallization occurs, and the sharp temperature spike caused by the release of the latent heat of melting is followed by a rapid cooling. At the low fluence, $F_{\text{abs}} = 14$ mJ/cm^2, Fig. 4(c), a brief (approximately 10 ps) superheating of the surface above T_m is too momentary for any significant propagation of the melting front, which is limited to less than 0.5 nm or a half of a cell in the spatial discretization in the model. Thus, we consider this fluence to be just below the melting threshold [see Fig. 4(d)]. As shown below through the analysis of cumulative diffusion length, the exposure of the solid film to high temperatures provides an opportunity for substantial atomic rearrangements, even though the diffusion is activated only during a few hundreds of picoseconds [Fig. 4(c)].

Since the A2-B2 transition occurs via atomic mixing between Fe- and Al-dominated planes proceeding through the vacancy-diffusion mechanism [23–25], we evaluate the cumulative mean-square displacement of Fe and Al atoms in the course of cooling after the end of resolidification as

$$\Delta^2 = 6\int_{t_1}^{t_2} D(T_s(t))dt, \tag{1}$$

where $D(T_s) = D_0\exp(-Q/RT_s)$ is the atomic diffusivity in the alloy with the prefactor $D_0 \approx 1.1 \times 10^{-3}$ m^2/s [23] and activation energy $Q = 241$ kJ/mol [23–25], $R = 8.314$ JK^{-1}mol^{-1} the universal gas constant, t_1 is the time of complete resolidification of the film [indicated by the arrows for two values of F_{abs} in Figs. 4(a)

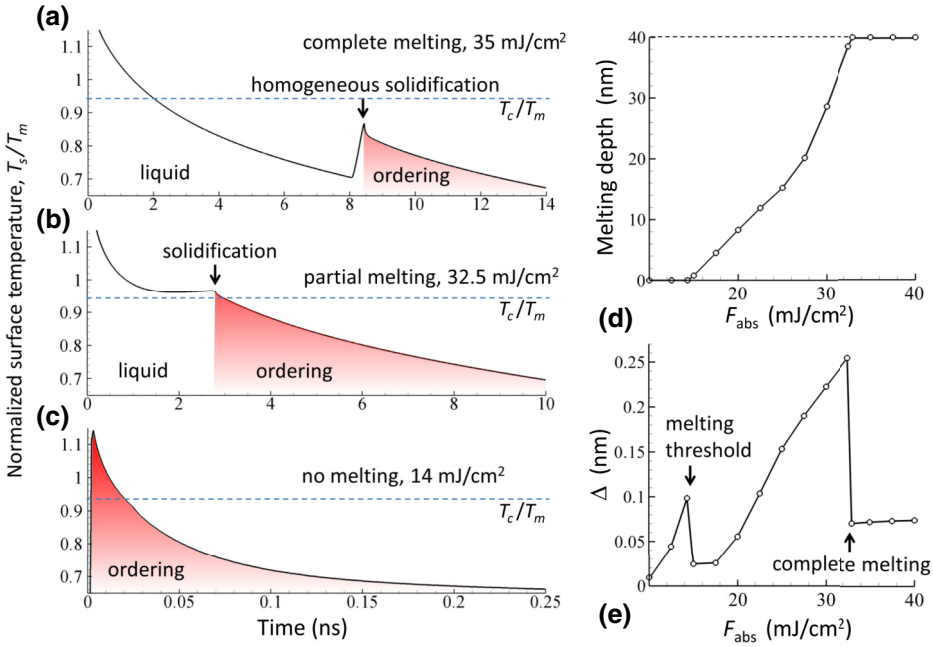

FIG. 4. Simulation results for a 40-nm $Fe_{60}Al_{40}$ film on a SiO_2(150 nm)/Si substrate irradiated by a 500-fs laser pulse. (a)–(c) Time evolution of the surface temperature, T_s, shown for three values of absorbed laser fluence, F_{abs}, that correspond to complete melting ($F_{abs} = 35$ mJ/cm^2), partial melting ($F_{abs} = 32.5$ mJ/cm^2), and no melting ($F_{abs} = 14$ mJ/cm^2) of the $Fe_{60}Al_{40}$ film. The surface temperature is normalized to the melting temperature $T_m = 1662$ K. The colored areas under the curves correspond to the solid state of the film surface, and the intensity of the color schematically represents the temperature dependence of atomic mobility. Arrows mark the times of complete solidification of the film. (d) Dependence of the maximum melting depth in the irradiated $Fe_{60}Al_{40}$ film on the absorbed fluence, F_{abs}. (e) The cumulative atomic diffusion length, Δ, in the solid film during the laser-induced temperature spike. In the melted alloy, the temperature decreases substantially below T_m (undercooling) before the resolidification of the film, leading to the sharp drops of atomic diffusion length at the surface melting threshold and at the threshold for complete melting of the film.

and 4(b)], while t_2 is the total duration of the simulation chosen to ensure a negligible change of Δ^2 upon further integration beyond t_2. Since the thermal energy redistribution within the 40-nm-thick metal film is rapid and takes approximately 100 ps, the temperature of the surface of the film, T_s, is used in the evaluation of the atomic diffusion length in the film. Note that Eq. (1) with parameters evaluated for the equilibrium vacancy concentrations provides a lower-end estimation of the atomic diffusion, as the rapid resolidification proceeding under conditions of strong undercooling below the melting temperature can generate a strong supersaturation of the film with vacancies [42].

As shown in Fig. 4(e), the dependence of the effective atomic diffusion length (Δ) on the fluence exhibits a sharp drop from its maximum value of 0.25 nm reached at $F_{abs} \approx 32$ mJ/cm^2 down to approximately 0.07 nm upon the complete melting of the $Fe_{60}Al_{40}$ film. This drop in Δ can be explained by strong undercooling of the melt prior to the complete resolidification [41]. When the film is only partially melted, the solidification proceeds through the propagation of solidification front from the solid part of the film, and the temperature stays at a relatively high level of approximately $0.94T_m$ until the end of the resolidification [see Fig. 4(b)]. The films melted to the full depth, on the other hand, resolidify through the rapid nucleation and growth of new crystallites activated when the molten metal cools down to approximately $0.7T_m$.The release of the heat of melting upon the solidification leads to a transient spike in the temperature of the film, e.g., up to $T(t_1) \approx 0.86T_m$ at $F_{abs} \approx 35$ mJ/cm^2 [Fig. 4(a)]. The diffusional reordering of the random solid solution generated by the solidification starts at this maximum temperature, but the film continues to cool, and the temperature rapidly drops down to the level where the diffusional reordering ceases. Indeed, from the value of $\Delta < 0.1$ nm calculated for F_{abs} above the threshold for complete melting to the full depth of the film, Fig. 4(e), we can estimate that only approximately 16% of atoms should change their positions per laser pulse, which can be not sufficient for any significant chemical reordered B2 phase. Therefore, the A2 phase and thus ferromagnetism can be expected to persist in the alloy after its cooling to RT. Note that a strong temperature dependence of the thermodynamic driving force for the A2-to-B2 ordering phase transformation does not allow us to quantitatively link the magnitude of Δ to the degree of the phase transformation produced by the laser irradiation. Nevertheless, it provides a useful measure of the extent of

the laser-induced atomic rearrangements in the solidified film, as a sufficiently large magnitude of Δ is a necessary (although not sufficient) condition for the transformation to the chemically ordered state.

The relatively low value of Δ produced upon irradiation by a single laser pulse below the melting threshold suggests that such a pulse is unlikely to induce complete A2-to-B2 phase transformation. Multiple laser pulses with the energy in each pulse not sufficient to induce melting and thus chemical disordering in the film can provide a sufficient cumulative time of the thermal spikes for the generation of a substantial amount of the B2 phase. The laser-induced reordering and, thus, erasing of the ferromagnetism has been demonstrated in our further experiments performed with magnetic microscopy imaging based on x-ray magnetic circular dichroism (XMCD) collected *in situ* [56]. These experiments indicate that even a single femtosecond pulse with intensity below the melting threshold is able to lower the XMCD contrast obtained with a higher intensity (above the melting threshold) pulse, while the magnetic signal is totally suppressed with approximately 10^4 pulses. These results are compatible with the values of cumulative mean-square displacement of Fe and Al atoms evaluated using Eq. (1). Alternatively, the reordering under standard thermal annealing at moderate temperatures, e.g., at $T = 773$ K, can be achieved within $t \sim a^2/D \approx 1.0$ s, where $D \sim 0.1$ nm^2/s at this T [23,24].

V. CONCLUSIONS

We find that thin $Fe_{60}Al_{40}$ films exhibit nonvolatile ferromagnetism at RT after irradiation by nanosecond or femtosecond laser pulses. This ferromagnetism can be erased under longer heat treatments at moderate temperatures (below melting), e.g., by standard thermal annealing, high-density electric current, irradiation by a longer laser pulse or a train of short laser pulses, all of which can lead to reordering of the atomic structure. After such treatment, the chemically disordered state (and thus RT ferromagnetism) can be regenerated through irradiation by a subsequent high-energy laser pulse. The simulations of laser interaction with $Fe_{60}Al_{40}$ films suggest that the ferromagnetic state is produced by rapid melting and resolidification of the $Fe_{60}Al_{40}$ film that traps the metastable chemically disordered state. We envision that cycling of the ferromagnetism in phase-change alloys could be utilized in the design of rewritable devices for long-term magnetic storage of information, e.g., in cryptography [63], ID cards [17], and archiving [64]. Using this approach in combination with near-field patterning techniques [3–8] for rewriting of nanoscale (<100 nm) magnets would have an advantage over conventional magnetic memories, since the problem of thermal fluctuations of magnetic moments below the superparamagnetic threshold [15] can be circumvented if one reads out, for instance, the magnetic permeability [17] rather than the orientation of magnetization in an information bit.

ACKNOWLEDGMENTS

The experimental part of this work is carried out with support by the Portuguese Foundation for Science and Technology (FCT) through the project PTDC/FIS/121588/2010, while computational and theoretical parts are supported by the National Science Foundation (NSF) through Grant No. CMMI-1436775. L.V.Z. also thanks the ITMO Fellowship Program. We thank R. Bali for suggesting this study, providing $Fe_{60}Al_{40}$ samples and involving N.I.P., M.H., M.V.S., and L.V.Z. in discussions and modeling of *in situ* experiments on laser-induced rewriting of the ferromagnetism in $Fe_{60}Al_{40}$ [56] as well as S. Cornelius for collecting GIXRD patterns. N.I.P. is also grateful to J. Lindner and J. Fassbender for fruitful discussions during his visit to the Helmholtz-Zentrum-Dresden-Rossendorf (HZDR).

[1] F. V. Bunkin, N. A. Kirichenko, and B. S. Luk'yanchuk, Thermochemical action of laser radiation, Sov. Phys. Usp. **25**, 662 (1982).

[2] A. K. Vorob'ev and C. Guo, Direct femtosecond laser surface nano/microstructuring and its applications, Laser Photon. Rev. **7**, 385 (2013).

[3] T. C. Chong, M. H. Hong, and L. P. Shi, Laser precision engineering: From microfabrication to nanoprocessing, Laser Photon. Rev. **4**, 123 (2010).

[4] Y. Tanaka, G. Obara, A. Zenidaka, M. Terakawa, and M. Obara, Femtosecond laser near-field nanoablation patterning using Mie resonance high dielectric constant particle with small size parameter, Appl. Phys. Lett. **96**, 261103 (2010).

[5] A. Plech, V. Kotaidis, M. Lorenc, and J. Boneberg, Femtosecond laser near-field ablation from gold nanoparticles, Nat. Phys. **2**, 44 (2006).

[6] Z. B. Wang, B. S. Luk'yanchuk, L. Li, P. L. Crouse, Z. Liu, G. Dearden, and K. G. Watkins, Optical near-field distribution in an asymmetrically illuminated tip-sample system for laser/STM nanopatterning, Appl. Phys. A **89**, 363 (2007).

[7] P. Royer, D. Barchiesi, G. Lerondel, and R. Bachelot, Near-field optical patterning and structuring based on local-field enhancement at the extremity of a metal tip, Philos. Trans. R. Soc. A **362**, 821 (2004).

[8] M. H. Kryder, E. C. Gage, T. W. McDaniel, W. A. Challener, R. E. Rottmayer, G. Ju, Y.-T. Hsia, and M. F. Erden, Heat assisted magnetic recording, Proc. IEEE **96**, 1810 (2008).

[9] R. Garcia, A. W. Knoll, and E. Riedo, Advanced scanning probe lithography, Nat. Nanotechnol. **9**, 577 (2014).

[10] R. Szoszkiewicz, T. Okada, S. C. Jones, T.-D. Lee, W. P. King, S. R. Marder, and E. Riedo, High-speed, sub-15 nm

feature size thermochemical nanolithography, Nano Lett. **7**, 1064 (2007).

[11] P. E. Sheehan, L. J. Whitman, W. P. King, and B. A. Nelson, Nanoscale deposition of solid inks via thermal dip pen nanolithography, Appl. Phys. Lett. **85**, 1589 (2004).

[12] S. R. Ovshinsky, Reversible Electrical Switching Phenomena in Disordered Structures, Phys. Rev. Lett. **21**, 1450 (1968).

[13] A. V. Kolobov, P. Fons, A. I. Frenkel, A. L. Ankudinov, J. Tominaga, and T. Uruga, Understanding the phase-change mechanism of rewritable optical media, Nat. Mater. **3**, 703 (2004).

[14] M. Wuttig and N. Yamada, Phase-change materials for rewritable data storage, Nat. Mater. **6**, 824 (2007).

[15] S. H. Charap, Thermal stability of recorded information at high density, IEEE Trans. Magn. **33**, 978 (1997).

[16] T. Takayama and H. Takagi, Phase-change magnetic memory effect in cation-deficient iron sulfide $Fe_{1-x}S$, Appl. Phys. Lett. **88**, 012512 (2006).

[17] J. Timmerwilke, S.-H. Liou, S. F. Cheng, and A. S. Edelstein, Rewriting magnetic phase change memory by laser heating, J. Phys. D: Appl. Phys. **49**, 165005 (2016).

[18] W.-D. Song, L.-P. Shi, X.-S. Miao, and C.-T. Chong, Synthesis and characteristics of a phase-change magnetic material, Adv. Mater. **20**, 2394 (2008).

[19] M. Hudl, P. Nordblad, T. Björkman, O. Eriksson, L. Häggström, M. Sahlberg, Y. Andersson, E.-K. Delczeg-Czirjak, and L. Vitos, Order-disorder induced magnetic structures of $FeMnP_{0.75}Si_{0.25}$, Phys. Rev. B **83**, 134420 (2011).

[20] J. Timmerwilke, J. R. Petrie, K. A. Wieland, R. Mencia, S.-H. Liou, C. D. Cress, G. A. Newburgh, and A. S. Edelstein, Using magnetic permeability bits to store information, J. Phys. D: Appl. Phys. **48**, 405002 (2015); J. R. Petrie, K. A. Wieland, J. M. Timmerwilke, S. C. Barron, R. A. Burke, G. A. Newburgh, J. E. Burnette, G. A. Fischer, and A. S. Edelstein, A multi-state magnetic memory dependent on the permeability of Metglas, Appl. Phys. Lett. **106**, 142403 (2015).

[21] A ferromagnetic entity with its diameter below the superpamagnetic threshold gives fluctuating stray fields, and so its magnetic signal is the telegraph noise; e.g., W. Wernsdorfer, E. Bonet Orozco, K. Hasselbach, A. Benoit, B. Barbara, N. Demoncy, A. Loiseau, H. Pascard, and D. Mailly, Experimental Evidence of the Néel-Brown Model of Magnetization Reversal, Phys. Rev. Lett. **78**, 1791 (1997). The signal amplitude should depend on the magnetization.

[22] Y. Yoshida, K. Oosawa, S. Watanabe, H. Kaiju, K. Kondo, A. Ishibashi, and K. Yoshimi, Nanopatterns induced by pulsed laser irradiation on the surface of an Fe-Al alloy and their magnetic properties, Appl. Phys. Lett. **102**, 183109 (2013).

[23] H. Mehrer, M. Eggersmann, A. Gude, M. Salamon, and B. Sepiol, Diffusion in intermetallic phases of the Fe-Al and Fe-Si systems, Mater. Sci. Eng. A **239-240**, 889 (1997).

[24] M. Eggersmann and H. Mehrer, Diffusion in intermetallic phases of the Fe-Al system, Philos. Mag. A **80**, 1219 (2000).

[25] R. Würschum, C. Grupp, and H.-E. Schaefer, Simultaneous Study of Vacancy Formation and Migration at High Temperatures in BZ-type Fe Aluminides, Phys. Rev. Lett. **75**, 97 (1995).

[26] G. P. Huffman and R. M. Fisher, Mössbauer studies of ordered and coldworked Fe–Al alloys containing 30 to 50 at. % aluminum, J. Appl. Phys. **38**, 735 (1967).

[27] Y. Yang, I. Baker, and P. Martin, On the mechanism of the paramagnetic-to-ferromagnetic transition in Fe-Al, Philos. Mag. B **79**, 449 (1999).

[28] L. E. Zamora, G. A. P. Alcázar, G. Y. Vélez, J. D. Betancur, J. F. Marco, J. J. Romero, A. Martínez, F. J. Palomares, and J. M. González, Disorder effect on the magnetic behavior of mechanically alloyed Fe_{1-x} Al_x ($0.2 \leq x \leq 0.4$), Phys. Rev. B **79**, 094418 (2009).

[29] A. Hernando, X. Amils, J. Nogués, S. Surinãch, M. D. Baró, and M. R. Ibarra, Influence of magnetization on the reordering of nanostructured ball-milled Fe-40 at.% Al powders, Phys. Rev. B **58**, R11864 (1998).

[30] E. Apiñaniz, F. Plazaola, J. S. Garitaonandia, D. Martín, and J. A. Jimenez, Study of the enhancement of the magnetic properties of $Fe_{70}Al_{30}$ in the order-disorder transition, J. Appl. Phys. **93**, 7649 (2003).

[31] R. Bali, S. Wintz, F. Meutzner, R. Hübner, R. Boucher, A. A. Ünal, S. Valencia, A. Neudert, K. Potzger, J. Bauch, F. Kronast, S. Facsko, J. Lindner, and J. Fassbender, Printing nearly-discrete magnetic patterns using chemical disorder induced ferromagnetism, Nano Lett. **14**, 435 (2014).

[32] E. Menéndez, M. O. Liedke, J. Fassbender, T. Gemming, A. Weber, L. J. Heyderman, K. V. Rao, S. C. Deevi, S. Suriñach, V. D. Baró, J. Sort, and J. Nogués, Direct magnetic patterning due to the generation of ferromagnetism by selective ion irradiation of paramagnetic FeAl alloys, Small **5**, 229 (2009).

[33] Y. Murakami, K. Niitsu, T. Tanigaki, R. Kainuma, H. S. Park, and D. Shindo, Magnetization amplified by structural disorder within nanometre-scale interface region, Nat. Commun. **5**, 4133 (2014).

[34] J. Bogner, W. Steiner, M. Reissner, P. Mohn, P. Blaha, K. Schwarz, R. Krachler, H. Ipser, and B. Sepiol, Magnetic order and defect structure of Fe_xAl_{1-x} alloys around x=0.5: An experimental and theoretical study, Phys. Rev. B **58**, 14922 (1998).

[35] E. Apiñaniz, F. Plazaola, and J. S. Garitaonandia, Electronic structure calculations of Fe-rich ordered and disordered Fe-Al alloys, Eur. Phys. J. B **31**, 167 (2003).

[36] P. Mohn, C. Persson, P. Blaha, K. Schwarz, P. Novák, and H. Eschrig, Correlation Induced Paramagnetic Ground State in FeAl, Phys. Rev. Lett. **87**, 196401 (2001).

[37] A. Galler, C. Taranto, M. Wallerberger, M. Kaltak, G. Kresse, G. Sangiovanni, A. Toschi, and K. Held, Screened moments and absence of ferromagnetism in FeAl, Phys. Rev. B **92**, 205132 (2015).

[38] It is found that an ordered (B2) $Fe_{60}Al_{40}$ thin (40 nm) film is weakly ferromagnetic with saturation magnetization of approximately 0.025 T; see, for instance, N. Tahir, R. Bali, R. Gieniusz, S. Mamica, J. Gollwitzer, T. Schneider, K. Lenz, K. Potzger, J. Lindner, M. Krawczyk, J. Fassbender, and A. Maziewski, Tailoring dynamic magnetic characteristics of $Fe_{60}Al_{40}$ films through ion irradiation, Phys. Rev. B **92**, 144429 (2015).

[39] P. Mohn, *Magnetism in the Solid State: An Introduction*, Springer Series in Solid-State Sciences, edited by

M. Cardona et al. (Springer-Verlag, Berlin, Heidelberg, 2003).

[40] S. I. Anisimov, B. L. Kapeliovich, and T. L. Perel'man, Electron emission from metal surfaces exposed to ultrashort laser pulses, J. Exp. Theor. Phys. **39**, 375 (1974).

[41] X. Sedao, M. V. Shugaev, C. Wu, T. Douillard, C. Esnouf, C. Maurice, S. Reynaud, F. Pigeon, F. Garrelie, L. V. Zhigilei, and J.-P. Colombier, Growth twinning and generation of high-frequency surface nanostructures in ultrafast laser-induced transient melting and resolidification, ACS Nano **10**, 6995 (2016).

[42] Z. Lin, R. A. Johnson, and L. V. Zhigilei, Computational study of the generation of crystal defects in a bcc metal target irradiated by short laser pulses, Phys. Rev. B **77**, 214108 (2008).

[43] E. D. Palik, *Handbook of Optical Constants of Solids* (Academic Press, New York, 1998).

[44] Z. Lin, L. V. Zhigilei, and V. Celli, Electron-phonon coupling and electron heat capacity of metals under conditions of strong electron-phonon nonequilibrium, Phys. Rev. B **77**, 075133 (2008).

[45] http://www.faculty.virginia.edu/CompMat/electron-phonon-coupling/

[46] A. Rudajevová and J. Buriánek, Determination of thermal diffusivity and thermal conductivity of Fe-Al alloys in the concentration range 22 to 50 at.% Al, J. Phase Equilib. **22**, 560 (2001).

[47] Y. Ruan, N. Yan, H. Z. Zhu, K. Zhou, and B. Wei, Thermal performance determination of binary Fe-Al alloys at elevated temperatures, J. Alloys Compd. **701**, 676 (2017).

[48] F. Stein and M. Palm, Re-determination of transition temperatures in the Fe–Al system by differential thermal analysis, Int. J. Mater. Res. **98**, 580 (2007).

[49] K. A. Jackson, The interface kinetics of crystal growth processes, Interface Sci. **10**, 159 (2002).

[50] Y. Ashkenazy and R. S. Averback, Kinetic stages in the crystallization of deeply undercooled body-centered-cubic and face-centered-cubic metals, Acta Mater. **58**, 524 (2010).

[51] *CRC Handbook of Chemistry and Physics*, edited by D. R. Lide, 84th ed. (CRC Press, Boca Raton, FL, 2003).

[52] P. E. Hopkins, R. N. Salaway, R. J. Stevens, and P. M. Norris, Temperature-dependent thermal boundary conductance at Al/Al_2O_3 and Pt/Al_2O_3 interfaces, Int. J. Thermophys. **28**, 947 (2007).

[53] E. Lampin, Q.-H. Nguyen, P. A. Francioso, and F. Cleri, Thermal boundary resistance at silicon-silica interfaces by molecular dynamics simulations, Appl. Phys. Lett. **100**, 131906 (2012).

[54] V. Lednev, S. M. Pershin, and A. F. Bunkin, Laser beam profile influence on LIBS analytical capabilities: single vs. multimode beam, J. Anal. At. Spectrom. **25**, 1745 (2010).

[55] C.-Y. You, I. M. Sung, and B.-K. Joe, Analytic expression for the temperature of the current-heated nanowire for the current-induced domain wall motion, Appl. Phys. Lett. **89**, 222513 (2006).

[56] J. Ehrler, M. He, M. V. Shugaev, N. I. Polushkin, S. Wintz, V. Liersch, S. Cornelius, R. Hübner, K. Potzger, J. Lindner, J. Fassbender, A. A. Ünal, S. Valencia, F. Kronast, L. V. Zhigilei, and R. Bali, Laser-rewriteable ferromagnetism at thin-film surfaces, ACS Appl. Mater. Interfaces **10**, 15232 (2018).

[57] L. V. Zhigilei, Z. Lin, and D. S. Ivanov, Atomistic modeling of short pulse laser ablation of metals: Connections between melting, spallation, and phase explosion, J. Phys. Chem. C **113**, 11892 (2009).

[58] J. Krüger, D. Dufft, R. Koter, and A. Hertwig, Femtosecond laser-induced damage of gold films, Appl. Surf. Sci. **253**, 7815 (2007).

[59] W. J. Boettinger and M. J. Aziz, Theory for the trapping of disorder and solute in intermetallic phases by rapid solidification, Acta Metall. **37**, 3379 (1989).

[60] W. J. Boettinger, L. A. Bendersky, J. Cline, J. A. West, and M. J. Aziz, Disorder trapping in Ni_2TiAl, Mater. Sci. Eng A **133**, 592 (1991).

[61] H. Hartmann, D. Holland-Moritz, P. K. Galenko, and D. M. Herlach, Evidence of the transition from ordered to disordered growth during rapid solidification of an intermetallic phase, EPL **87**, 40007 (2009).

[62] S. Bysakh, P. K. Das, and K. Chattopadhyay, Metastable microstructures in laser-ablation-deposited Al-Fe thin films, Philos. Mag. A **81**, 2689 (2001).

[63] *Cryptography and Coding*, edited by C. Boyd, Proc. of 5th IMA Conf. (Cirencester UK, December 1995), Springer, 1995.

[64] J. W. C. van Bogart, *Magnetic Tape Storage and Handling: A Guide for Libraries and Archives* (Washington DC and St Paul, MN: Commission on Preservation and Access and National Media Lab, 1995).